Materials Advances

ROYAL SOCIETY OF CHEMISTRY

PAPER

View Article Online
View Journal

Cite this: DOI: 10.1039/d5ma00962f

Production of assorted nanoparticle structures using silver–cerium redox chemistry for inactivation of coronavirus

Craig J. Neal, *[a] Muhammad Hassan Mehmood Kalyar,[b] Elayaraja Kolanthai,[a] Maria V. Bolen,†[b] Griffith D. Parks[b] and Sudipta Seal *[ac]

Received 26th August 2025,
Accepted 26th December 2025

DOI: 10.1039/d5ma00962f

rsc.li/materials-advances

Nanoscale cerium oxide is a material of interest for biomedical applications due to the breadth of therapeutic activities demonstrated in research literature. Further, these activities have been shown to be tunable, with control of material surface properties achievable through various wet chemical syntheses. In our previous studies, we have demonstrated unique antiviral performance for nanoscale cerium oxide formulations and related these performances to material properties. In the presented work, we have expanded the space of silver–cerium oxide compositions for use in virus inactivation: examining the effect of synthesis parameters on particle character and of core–shell nanoparticle formulations effects on human coronavirus mitigation. Comparisons among these formulations and a previously reported silver-decorated ceria formulation are made and related to relevant material properties.

1. Introduction

Cerium oxide (ceria) is a material of great significance for industrial catalysis, owing to its oxygen buffering (or storage) capacity and associated redox cycling at cerium sites (Ce^{3+}/Ce^{4+}).[10,11] These changes in material composition are produced and facilitated by the formation or healing of (near-)surface oxygen vacancies as

$$2Ce_{Ce}^{\times} + O_{o}^{\times} \leftrightarrow V_{o}^{\bullet\bullet} + 2Ce_{Ce}^{\prime} + \frac{1}{2}O_2 \quad (1)$$

in Kröger–Vink notation; with $Ce_{Ce}^{\prime}$ and $Ce_{Ce}^{\times}$ representing the formal redox states Ce^{3+} and Ce^{4+}, respectively. For nanoscale confined cerium oxide phases, it has been shown that formation of oxygen vacancies is promoted, occurring under lower formation energies and thereby, leading to an improved catalytic performance in select publications.[1] In many such studies, ceria thin films have been produced and modified with nanoscale silver phases as a means of producing activated oxygen intermediates.[2]

Several studies of silver–ceria nanoscale composite/(photo)-catalyst-active support structures have been reported in literature.[3–6] It is argued that atmospheric components, especially oxygen, are activated at elevated temperatures and undergo reaction with ceria adsorbed organic species which are transformed to chemical products upon ceria redox cycling. It has also been suggested that cerium is kept at a reduced chemical state at the interface between ceria and silver phases and that oxygen transferred from the silver surface, or electrons transferred through the silver bulk, restore initial cerium redox state conditions.[7,8] These results have been observed in several studies both experimentally and theoretically.[4] In other studies, nanoparticle silver–ceria architectures have been produced and studied as catalysts in chemoselective reduction reactions (*e.g.*, of unsaturated aldehydes, epoxides).[9,10]

In a work published by Kayama *et al.*, core–shell type silver–ceria nanomaterial compositions were produced for soot oxidation applications.[11] Interestingly, the authors note a 'rice-ball' structure (average reported diameter: ~100 nm) for the formulations, noting that the particles possess a comparatively less granular silver core, surrounded by a less uniform polycrystalline, granular shell comprised of ceria crystallites. Further, it was reported by the authors that the observed high efficiency soot oxidation may be ascribed to the structure: with the low-density character of the ceria shell potentially allowing diffusion to/from the silver phase while protecting silver from sintering or other modes of inactivation. While this observation is highly valuable for surface catalysis considerations, the synthesis chemistry may be of more general interest for expanding the potential scope of materials designs and applications.

Hydrothermal synthesis of silver–ceria rice-ball formulations was performed in an ammonia solution; with the

[a] Materials Science & Engineering Department, Advanced Materials Processing and Analysis Center (AMPAC), University of Central Florida, Orlando, FL 32816, USA. E-mail: Craig.Neal@ucf.edu, Sudipta.Seal@ucf.edu
[b] Burnett School of Biomedical Sciences, College of Medicine, University of Central Florida, Orlando, Florida 32827, USA
[c] Biionix Faculty Cluster, College of Medicine, Nanoscience Technology Center, University of Central Florida, Orlando, Florida 32827, USA
† Current address: NSF REU; Nova Southeastern University, Fort Lauderdale, FL, 33328, USA.

dissolution of silver-rich secondary particle phases and the oxidation of cerium ascribed to formation of $[Ag(NH_3)_2]^+$ complexes as

$$Ce(OH)_3 + [Ag(NH_3)_2]^+ + H_2O \rightarrow Ag^0 + Ce(OH)_4 + 2NH_3 + H^+ \quad (2)$$

In an earlier study, we reported the formation of silver-decorated ceria nanoparticle formulations through an alkaline precipitation and ammonia-mediated etching procedure to form the above-noted diamine complex.[12] In the same study, hydrogen peroxide was used, in a similar manner, to preclude formation of contaminant secondary phases while promoting silver/cerium redox reactions leading to formation of silver–ceria nanocomposite structures and no appreciable secondary pure phase (secondary) particle formation. Particle formulations from each of these syntheses were then evaluated for their distinct efficacies towards specific virus families; with representative viruses consisting of enveloped and non-enveloped structures, as well as viruses with RNA and DNA genomes.[12,13] The results highlighted the value of the nanomaterial surface in the application and suggest the potential for tuning (optimizing) the interaction through modification of the surface composition. Further, the character of particles produced by both methods implicate an influence of cerium–silver redox-mediated interactions on the observed composite formations.

In the current work, we aimed to further study the influence of redox reactions in the cerium–silver–ammonia chemical system on particle composition and phase distributions/architectures. Toward this end, multiple studies into the kinetics of diamine complex formation and of cerium–silver interactions were performed. It was found that on co-dissolution, aqueous solutions of cerium and silver nitrate undergo spontaneous complexation which produces a substantial effect on particle product character. Additionally, it was demonstrated that the influence of Ce : Ag ratio from initial reactant concentrations led to variations in particle phase architecture, size, and number. Influences of these differences among silver–ceria formulation particle characters are highlighted by their efficacies in the inactivation of human coronavirus OC43. Results from these syntheses and biomedical studies build on results from our previously reported studies, with our current formulations outperforming our previous formulation ($p < 0.05$) inducing an $\sim$3 log reduction in OC43 virus titer relative to control after 4 h exposure.[12,13]

2. Materials and methods

2.1 Material characterization

All UV-vis spectrophotometry measurements were performed using a PerkinElmer spectrophotometer; with data acquired over the range 220 to 600 nm using quartz crystal cuvettes. X-ray diffraction measurements were performed on powder samples using an Empyrean Panalytical diffractometer with CuKα (1.54 Å) radiation source. Data was analyzed using XPert Highscore software. High-resolution transmission electron microscopy images were collected at the University of Central Florida (Phillips, Tecnai, 300 kV; materials characterization facility) and the University of Florida (FEI Talos F200i, 200 kV; nanoscale research facility). Samples were prepared by drop-casting and drying from suspension onto lacey carbon film-coated, copper TEM grids (SPI) Images were collected at several magnifications. Scanning TEM imaging, HAADF, and selected area electron diffraction measurements were collected using the Talos hrTEM at the University of Florida. Inductively coupled mass spectrometry measurements were performed to measure cerium and silver concentrations for assorted material formulations at the Plasma Chem Lab at the University of Georgia, Athens (Center for Applied Isotope Studies). Particles were characterized for superoxide dismutase-mimetic activities using an SOD Assay kit (Dojindo Molecular Technologies), per manufacturer's instructions. Measurements were all performed in triplicate.

2.2 General silver–ceria synthesis procedure

All silver–ceria formulations for the presented study were produced by a similar synthesis protocol adapted from ref. 11, though with variations for mechanism and optimization studies (detailed in relevant, later subsections) noted by symbol (*); apart from AgCNP1: produced by a previously published protocol (detailed in brief, later in Section 2.4).[12]

2.71 g of cerium nitrate hexahydrate (99.999% purity, Sigma Aldrich) was dissolved in 4 mL de-ionized water (diH_2O; >20 MΩ, Barnstead Nanopure) and a relevant amount (based on intended composition, mole ratio of Ce : Ag, detailed below) of aqueous silver nitrate (99% purity, Sigma Aldrich). The solution was completed to 8.036 mL with diH_2O under magnetic stirring at 250 rpm at standard pressure and temperature (*) for a fixed time. Following this, the solution stir speed was increased to 350 rpm and 7.26 mL of an ammonia solution (35.6 wt% of a 25 wt% ammonia solution) was added quickly drop-wise. The solution was left stirring for 1 minute and then quickly added to a 23 mL volume Teflon-lined, stainless steel autoclave and sealed. The solution was then kept at 120 °C for 15 minutes in a pre-heated muffle furnace. Subsequently, the autoclave was cooled under a stream of cool water until cool to the touch ($\sim$5 minutes).

2.3 Silver–ceria particle purification procedure

The collected solution was then washed 4× with repeated centrifugation at 12 000 rpm for 10 minutes and solvent (supernatant) replacement with fresh de-ionized water. After washing, the pelleted sample was re-dispersed in a small volume of de-ionized water and dried overnight at 60 °C in a glass Petri dish. The dried sample was collected by scraping and powdered using mortar and pestle. Samples were then stored in borosilicate 5 mL vials until further use or characterization.

2.4 Synthesis of AgCNP1, silver–ceria control formulation

This synthesis is reported in an earlier work.[12] Briefly, 1.74 g of cerium nitrate hexahydrate was dissolved under stirring at $\sim$250 rpm on a magnetic stir plate in 40 mL of diH_2O.

A 10 mL solution containing 0.17 g of aqueous silver nitrate was then added to the aqueous cerium nitrate solution and allowed to mix for several minutes. From here, 10 mL of a 0.4 M sodium hydroxide solution was added quickly drop-wise to the cerium/silver solution under stirring at ~450 rpm. After 4 h, the resulting solution was washed by centrifugation 4× by replacing supernatant with fresh diH_2O. Finally, the purified material was re-suspended in diH_2O and ultra-sonicated in an ultrasonication bath to promote dispersion. To remove secondary, silver-rich particle phases, the purified solution was subsequently treated with a concentrated ammonium hydroxide solution (finally concentration: 3 wt%) under moderate stirring for 24 h. The solution was washed and isolated as denoted earlier in the synthesis.

2.5 Influence of silver–cerium redox interactions at auto-genic pH on particle product

Measurements of silver and cerium redox kinetics were performed keeping a 1 : 1 mole ratio of silver to cerium (nitrate) solution under stirring at 250 rpm. Sample aliquots (20 μL) were collected every 10 minutes up to 60 minutes. Measurements were performed at two dilution values to best resolve peak absorbance intensities of time-varying (and inversely related) magnitudes near 250 and 300 nm.

2.6 Synthesis of nanostructure formulations of varying silver-to-cerium mole ratios

Produced material formulations were synthesized by the procedure outlined in Section 2.1, though with varying silver to cerium molar ratios, and subsequently purified by the procedure detailed in Section 2.3 with aqueous cerium and silver nitrate mixed for 60 minutes. Formulations produced for the study include cerium to silver molar ratios of 1 : 1.5, 1.2, 1.0, 0.5, 0.2, and 0.1. Following initial characterizations, only formulations produced from the ratios 1 : 1.2, 1 : 0.5, and 1 : 0.2 were used for further studies; noted hereafter as formulations −1.2, 0.5, and 0.2, respectively. To probe the influence of the chemical process identified in time-dependent UV-vis measurements, a companion series of materials were also synthesized by stirring for only 2-minutes and otherwise identical synthesis and work-up procedures (for ratios 1 : 1.2, 1 : 0.5, and 1 : 0.2 noted hereafter as formulations −*k*1.2, *k*0.5, and *k*0.2, respectively).

2.7 Propagation of human coronavirus OC43

Rhabdomyosarcoma (RD) cell cultures were grown and maintained in Dulbecco's modified Eagle medium (DMEM; Gibco, Thermo Fisher Scientific) supplemented with 10% heat-inactivated fetal bovine serum (HI FBS) at 37 °C with 5% CO_2. Human coronavirus OC43 (ATCC VR-1558) was propagated in HCT-8 (ATCC HRT18) cells cultured at 33 °C. Supernatants were collected at 4 days post-infection (dpi), followed by centrifugation and supplemented with a 1 : 20 dilution of bovine serum albumin fraction V (BSA; 7.5% solution, Fisher Scientific). Virus-containing media was aliquoted, flash-frozen in liquid nitrogen, and stored at −80 °C.

2.8 Nanoparticle treatments of virus suspensions

Viral titers were determined by 50% tissue culture infectious dose ($TCID_{50}$) assay using confluent RD cell monolayers seeded in 96-well plates (Falcon, Thermo Fisher Scientific). Virus samples were serially diluted 10-fold in DMEM containing a 1 : 20 dilution of BSA and incubated with cells for 1 hour at 33 °C. Following infection, cells were washed with PBS and overlaid with DMEM supplemented with 2% HI FBS. After 4 days at 33 °C, cells were washed with PBS and fixed/stained with a 1% crystal violet solution containing 20% ethanol, 3.7% formaldehyde, and PBS for 30 minutes at room temperature. $TCID_{50}$ values were calculated using the Spearman–Kärber method. All measurements were performed in triplicate (n = 3) and are presented as the calculated mean ± standard deviation. Statistical significance was assessed *via* *t*-test analyses with respect to $TCID_{50}$ values for control silver–ceria formulation (noted as AgCNP1).

3. Results and discussion

A hydrothermal synthesis was considered for the production of silver–cerium oxide nanoparticle formulations with the use of ammonium hydroxide to directly preclude formation of secondary particles. The procedure is adapted from one presented by Kayama *et al.*, which resulted in core–shell particles with limited dispersity in particle character (size, shape, composition). The current studies examine the influence of varying cerium and silver precursor ratios and mixing time on average particle character; especially, silver and cerium oxide phase densities, average particle size, and particle morphologies.

Particle formulations were produced (Fig. 1A) with varying initial mole ratios of silver and cerium (Ag : Ce) (Fig. 1B). The ratio values were chosen to consider phase character and distribution for starting concentrations varied from 1 : 0.2 to :1.2 (*i.e.*, silver-lean, silver-rich initial solutions; final silver to cerium ratios presented in Fig. 1B and C and discussed in Section 3.3). Results were interpreted with respect to the influence of cerium oxidation by aq. $[Ag(NH_3)_2]^+$ complexes in a 1 : 1 mole ratio and by dissolved oxygen (natural aeration). In particular, particle number, silver : cerium oxide phase ratio, and particle morphological character were evaluated.

On mixing aqueous cerium and silver nitrate solutions, no obvious change in solution character typically occurred. However, it was observed that changing the time allowed for mixing resulted in solutions of various colors, with all other synthesis conditions kept fixed. Therefore, the influence of this mixing time was first considered.

3.1 Silver–cerium (oxide) interactions in absence of ammonia at auto-genic pH

Silver and cerium nitrate solutions were mixed at a final mole ratio of 1 : 1 and concentrations identical to the standard synthesis. UV-Vis spectra (Fig. 2) collected for this solution at regular timepoints (10 min intervals, from 0 to 60 min) reflect a spontaneous change in material redox states, with absorption

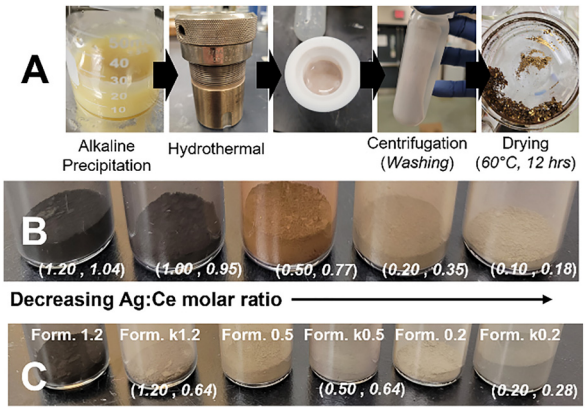

Fig. 1 Synthesis of assorted silver-modified cerium oxide formulations. All syntheses for the current studies were produced by wet chemical, hydrothermal syntheses at 150 °C. Samples dried to powders at 60 °C (B) and (C) highlight the substantial influence of silver to cerium precursor ratios (Ag : Ce ratio decreases from left to right across (B)) and mixing time ((C), decreasing Ag : Ce ratio from left to right, formulations 1.2, 0.5, and 0.2 for 60 minute and *k*1.2, *k*0.5, and *k*0.2 for 2 minute mixing time) on particle character. Initial and final (as measured by ICP-MS) mole ratios of silver to cerium are provided in overlay (''initial, final'').

near 298 nm (characteristic of Ce^{4+}) varying over the mixing period (Fig. 2A). The change in absorption intensity, for fixed material concentrations, suggests some change in redox state and potentially complexation. It should be noted that oxidation of cerium in absence of silver under these conditions (standard temperature and pressure, pH: ~3.5), and within this time period, is negligible.

Changes in peak relative intensities begin immediately and change up to approximately 1 h mixing time. From here, changes continue, though at a substantially lower rate. It should be noted, however, that while changes in absorption intensity near 298 nm, associated with Ce^{4+}-related transitions are mirrored by a proportional change in absorption near 252 nm, associated with Ce^{3+}-related transitions, silver (Ag^{+}) shows absorption near 300 nm as well: confounding attribution solely to cerium redox. However, these spontaneous processes may have implications on the synthesis product, in the least potentially adding to dispersity in material character. Therefore, syntheses were performed, on a subset of the initially synthesized formulations, with mixing occurring for 2 or 60 minutes (Fig. 1C) prior to ammonium hydroxide addition and hydrothermal processing. The subset was chosen to provide additional insight into conclusions produced in previous studies and to probe the particle formation mechanism; specifically, formulations produced from a 1 : 1.2, 1 : 0.5, and 1 : 0.2 cerium to silver mole ratio were considered as formulations 1.2, 0.5, and 0.2, respectively (for syntheses mixed for 60 minutes and with corresponding syntheses mixed for 2 minutes noted as formulations *k*1.2, *k*0.5, and *k*0.2).

3.2 Influence of mixing time on particle product material characters: spectroscopy

Changes in UV-vis spectra discussed in the preceding section suggested a potential influence of mixing time on solution component speciation and final particle product character. This suggestion is further supported by visual examination of collected sample powder coloration (Fig. 1C). Coloration will be the product of absorption by silver and cerium in unique crystal environments and of their respective, consequent chemical state distributions.

UV-Vis spectra for formulations 1.2, 0.5, and 0.2 and *k*1.2, *k*0.5, and *k*0.2 are presented in Fig. 2B. All formulations show a broad peak spanning the visible region, as suggested by their dark colorations. Interestingly, all formulations, excluding formulation 1, appear to show peak maxima centered near 400 nm. It is noteworthy that the spectra for each test group are unique, implicating silver content on the final particle chemical state distributions and consequent electronic structure. Interestingly, relative intensities for peaks in regions ascribable to cerium oxide and for silver do not show a clear trend. However, the breadth of peaks, peak shifts associated with quantum confined electronic states, and potential for signal overlap contraindicate this analysis as a metric for comparing compositions across formulations.[14]

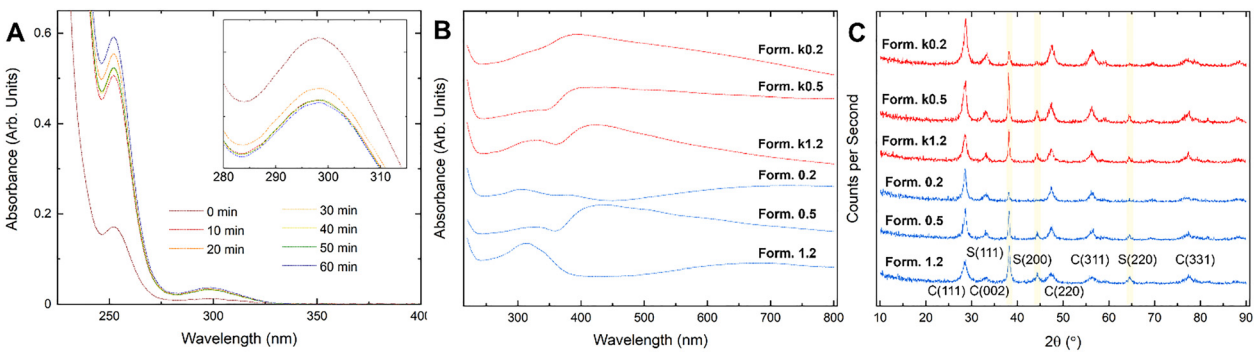

Fig. 2 Silver–cerium oxide nanoparticle formulation phase composition and character. UV-Vis spectrophotometry measurements at fixed time intervals (10 min) over a 60 minute period (A) highlight changes in particle precursor character with mixing time (inset: magnified image of the absorption between 280 and 315 nm). Changes in abosprtion are time-sensitive and non-monotonic. UV-Vis spectra for formulations 1.2, 0.5, and 0.2 and *k*1.2, *k*0.5, and *k*0.2 (B) are presented and suggest substantial difference in silver phase character (peak character at wavelengths >400 nm). X-ray diffraction (XRD) measurements (C) show peaks associated with both cerium oxide (fluorite symmetry, indexed to ICSD 55284) and metallic silver (body-centered cubic symmetry, indexed to ICSD 44387) for all formulations.

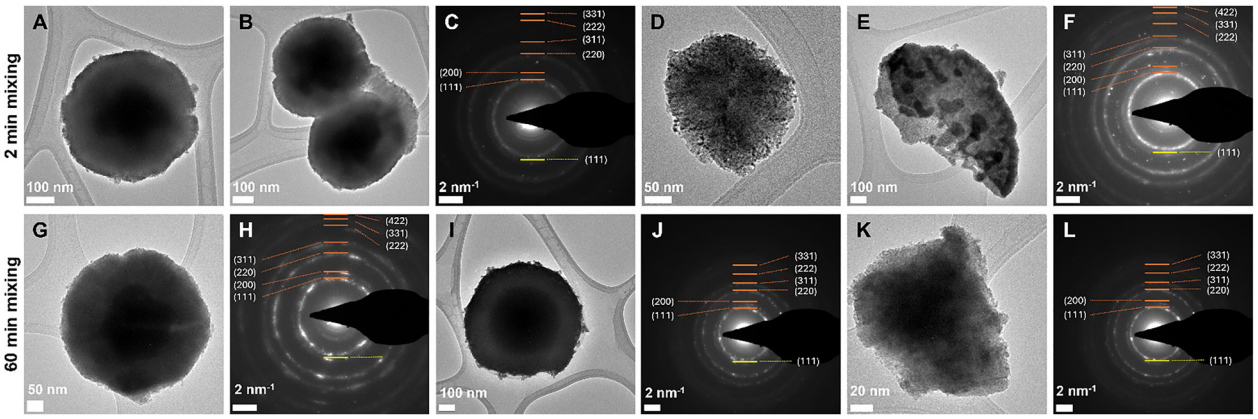

Fig. 3 High-resolution transmission electron microscopy images of particles from formulations with two or sixty minutes of stirring. Mixing time (top row: 2 minutes, formulations *k*1.2 and *k*0.2, from left to right, respectively; bottom row: 60 minutes, formulations 1.2, 0.5, and 0.2, from left to right, respectively) for cerium and silver precursors show substantial influence on particle morphology, phase compositions. Particles from formulation *k*1.2 (A) and (B) appear as individual (A) as well as aggregates of core–shell particles (B). Particles from formulation *k*0.2 (D) and (E) appear irregular, with silver-rich regions appearing at higher number densities throughout a given particle as compared to formulations *k*1.2 and *k*0.2. Particles from formulations 1.2 (G) and 0.5 (I) appear as large core–shell (silver–ceria, respectively) nanostructures, while particles from lower Ag : Ce ratio formulation 0.2 (K) appear less regular and with silver phases more disperse. Selected area electron diffraction(SAED) measurements reflect a presence of fluorite structured cerium oxide and body-centered cubic structure for particles from all formulations.

Comparing XRD diffractograms across formulations 1.2, 0.5, and 0.2 and their respective *k*-series correlates, we observe distinctions which can be related to individual synthesis details (Fig. 2C). All spectra evidence the presence of both cerium oxide (fluorite symmetry, indexed to ICSD 55284) and silver (body-centered cubic symmetry, indexed to ICSD 44387). For cerium oxide, five peaks are fit to all experimental spectra; namely, (111), (002), (220), (311), and (331). For silver, three peaks were fit; namely, (111), (200), and (220). Peak broadening is evident for all peaks and ascribed to the nano-scale character of all phases in the final material; full-width half-max values were computed for each formulation. The observed differences in spectroscopic measurements are better understood by considering the structural differences of formulation particles under high resolution transmission electron spectroscopy imaging.

3.3 Influence of mixing time on particle product material characters: microscopy

High-resolution transmission electron microscopy (TEM) (Fig. 3) imaging demonstrates the substantial influence of both mixing time (Fig. 3A, B and D, E) and Ag : Ce molar ratio (Fig. 3G, I and K) (Fig. S1). Selected-area electron diffraction (SAED) measurements for both test group (Fig. 3C, F and H, J, L for the 2 and 60 minute mixed samples) formulations corroborate observations in XRD, with diffraction spots appearing as rings due to the nanoscale dimensions of both silver and cerium oxide phases. Fitting of diffractions rings confirms a fluorite and body-centered cubic structure for silver and cerium oxide phases, respectively, for all formulations.

Scanning TEM (STEM) and high-angle angular dark field imaging (HAADF) (Fig. 4) analysis was performed for particles from a 1 : 1 Ag : Ce synthesis, as a representative sample. Spectroscopic (EDS) analysis confirms a core–shell morphology with silver localized to the particle core and cerium oxide (cerium, oxygen, silver, and their compositions in Fig. 4B, C, D, and F, respectively) comprising the shell structure. Imaging at this lower magnification (Fig. 4E) additionally demonstrates the limited dispersity in particle size and morphology in this formulation.

In comparing particles from formulations having common silver and cerium initial concentrations, we observe an approximate consistency in general morphology. Particles from formulations 1.2 and *k*1.2 appear as core–shell structures, with a silver core enclosed by highly poly-crystalline cerium oxide. Particles from formulation 0.5 similarly appear largely as core–shell type structures, though with the additional presence, in limited population number, of less regular structures

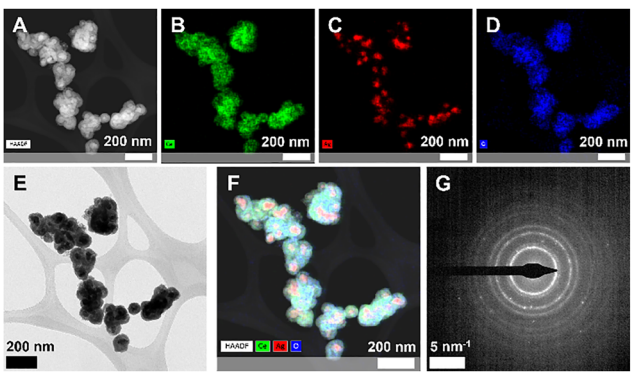

Fig. 4 Scanning transmission electron microscopy (STEM) and high-angle anular dark field (HAADF) imaging of silver–cerium oxide 1 : 1 formulation. HAADF imaging (A) highlights spatial distributions of phase components. Elemental distributions of cerium (B), silver (C), and oxygen (D) showing spatial distribution into core and shell particle morphologies. hrTEM (E) and composition of elemental distribution measurements (F) are presented for comparison. Selected area electron diffraction (SAED) (G) ring structures highlight the nano-scale dimensions of fitted cerium oxide (fluorite) and metallic silver components (body-centered cubic).

(ellipsoidal, 1D). The majority of particles observed from formulations 0.2 and *k*0.2 appear less regular, with the lower silver content relative to cerium during synthesis appearing to produce multiple silver-rich regions throughout individual composite (AgCNP) particles. Interestingly, in addition to the apparent increased number of silver-rich regions for these particles, silver phases appear irregular in shape. The observed character is more pronounced for formulation *k*0.5, though particles from formulation 0.5 similarly show a more even distribution of silver phases throughout particles and potentially at the particle surface. Despite the observed similarity in general morphology for formulations containing common silver and cerium initial concentrations, there is an additional pattern of smaller particle size for formulations mixed for longer times.

Interestingly, we observe some tendency for elongated, ellipsoidal particles to varying extents in all formulations. For smaller core–shell structured particles, this tendency is less obvious, with the majority of *k*1.2 particles possessing a slight morphological eccentricity (ratio of minor to major axis diameter in TEM image data; avg. 0.89). However, imaged particles evidence a long axis terminated at either end by apparent breaks in the cerium oxide shell. These defects and particle morphology are consistent and are potentially ascribed to the morphology of the silver core. Diffraction measurements evidence a high intensity of (111) planes for all samples, suggesting a tendency toward octahedral or prismatic morphologies. Further, presence of multiple silver cores within a given particle suggests a potential for assembled multi-particle, hierarchical assemblies which may produce the observed trend. In support of this description, smaller particles observed in formulation 1.2 appear more regular (eccentricity: 0.97, relative to 0.89 for *k*1.2). Further, a smaller population of rod-shaped particles are seen in formulation *k*1.2 (Fig. 5C). This observation, occurring for the formulation pair possessing the highest silver to cerium ratio, additionally suggests an assembly behavior for silver, albeit likely for silver phases forming with limited cerium oxide surface density. Additionally, in our previous work which produced and characterized a silver–ceria formulation synthesized through the addition of hydrogen peroxide to aqueous solutions of silver and cerium nitrate, Janus-type particle architectures were observed.[12] A similar particle character was observed in another published study with citrate present as a reducing agent.[15] This common observation, along with the observation of shell defects at opposing ends of larger core–shell particles in the current study suggest ceria deposition at the silver surface may be a rate-limited or energetically unfavorable process. As suggested in other publications, deposition of silver may be promoted at the growing silver surface upon redox reaction with cerium; therefore, processes which reduce the total interface area will predominate. A growth mechanism wherein silver deposition and cerium oxide growth occur at distant sites (*e.g.*, opposite-side reactions) would result in the Janus-type structure; with aggregation, oriented assembly of such sub-units to larger core-shells occurring subsequently. Alternatively, a preferred deposition of ceria at specific silver facets would promote silver growth which increases surface density of these facets and, thereby, promotion of irregular particle morphologies (*e.g.*, the ellipsoidal (lemon-shaped) morphology with ceria-lean regions at opposing ends observed for larger core-shells and appearance of rod-like shapes, Fig. 5C). Interestingly, average crystallite diameters, as determined by analysis of XRD peaks *via* the Scherrer equation, for ceria and silver phases are similar for formulations *k*1.2–*k*0.2 (approximately 8 and 20 nm for ceria and silver, respectively), though vary appreciably with increasing silver to ceria ratio for formulations 1–3 (ceria: 6.418, 6.813, 9.419, 9.732; silver: 14.95, 18.67, 23.32, 22.97;for 1 : 1.2, 1.0, 0.5, and 0.1, respectively). This result suggests a significant interaction between cerium and silver, as further evidenced in UV-vis spectra (Fig. 2A). For 1 : 1 Ce : Ag ratio particles (Fig. 4), the particles are smaller in size and more regular, suggesting a case where equivalent proportions of reactant lead to regular-shaped morphologies. Interestingly, particles produced from these precursor ratios are on average substantially smaller in diameter (~85 *v.* ~450 nm), relative to core–shell structures produced from other formulations. This result highlights the interdependance between composite formation and morphology. Particles from formulation 0.2 are more similar to those produced by an alternative synthesis, at similar Ag : Ce ratios, published in our earlier work (AgCNP1 here, Fig. 5A). On etching a sample from formulation 0.2 in concentrated ammonium hydroxide, we observe an apparent presentation of silver phases at the material surface (Fig. S1). It is proposed that silver-rich regions of the particles may be etched and redeposited from aq. $[Ag(NH_3)_2]^+$ complexes; especially, at surface defects, such as oxygen vacancies, where Ce^{3+} sites localize and are available to oxidize silver from the complex.[16] Results from ICP-MS (Fig. 1B and C) further highlight a distinction between formulations produced from a starting silver : cerium ratio greater or less than 1. Ratio of 1.0 or higher produced particles of approximately 1 : 1 silver : ceria (1.04 and 0.95 for initial ratios of 1.2 and 1.0, respectively), corroborating the initial result of Kayama *et al.*[11] Interestingly, formulations produced from initial ratios less than 1.0, produced particles which were all nearly 50% richer in silver than the initial ratios (0.77, 0.35,

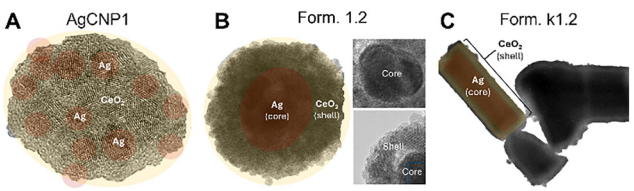

Fig. 5 Effect of synthesis conditions and parameters on particle nanostructure products. Varying synthesis conditions, with common reagents, resulted in synthesis of assorted nanostructures which can be represent-edgenerally as silver-decorated ceria (A), silver–ceria core–shell (B), and 1-dimensional core–shell structures (C). Relations between synthesis conditions and resultant particle characters provide insight into formation mechanism and potentially suggest future routes for controlled snythesis. Dispersion in particle size, morphology, and architecture (compare C to Fig. 3D and E), especially in the case of low mixing time samples, highlight the sensitivity of the particle character to synthesis conditions.

0.18 for initial ratios of 0.50, 0.20, and 0.10, respectively). This result suggests that the redox reaction between cerium and silver occurs more readily than the formation of ceria by other reaction pathways under the utilized synthesis conditions. This observation may also relate to the observed, relative irregularity and more complex morphology of particles from these formulations. Formulation *k*1.2 demonstrated a substantial decrease in silver : cerium ratio which was similar to that observed for *k*0.5 (0.64 for both), while the ratio for formulation *k*0.2 showed a slight enrichment (0.28): similar to formulation 0.2. These results further support the trends noted above.

In aggregate, our studies have highlighted a substantial sensitivity of particle character to synthesis conditions: with particle compositions varying in phase number, morphologies, and dimensionalities (Fig. 5). This control over morphology shows potential for further investigation of AgCNP virus inhibition activities. In the following studies we consider the virus-inactivation efficacies for particles from our previous studies (AgCNP1, Fig. 5A), formulation 1.2 (Fig. 5B), formulation 0.5, and formulation 0.2.

3.4 Virus inactivation by silver–ceria formulations: effects of phase distributions and phase structures

To evaluate the ability of nanoceria and AgCNPs to inactivate human coronavirus OC43, reactions were prepared with an initial concentration of $\sim 10^5$ infectious units ($TCID_{50}$) per mL of virus and 0.2 or 0.77 mg mL^{-1} nanoparticle treatments and were performed in triplicate (Fig. 6A). Nanoparticle treatment concentrations, for these studies, were chosen based on dose-dependence studies from our prior studies of similar silver–ceria nanoparticles to allow direct comparison to results from these studies.[12] This initial titer served as the time zero infectivity reference. Incubation of OC43 with buffer alone resulted in negligible loss of infectivity (Fig. 6A), consistent with previous findings regarding coronavirus stability in aqueous environments. Unmodified nanoceria formulations had minimal impact on viral titers, which remained at more than 5×10^4 $TCID_{50}$ per mL. In contrast, treatment with AgCNP1 and formulation 3 for 1 hour led to a 1-log reduction in viral titer, while formulation 1 and formulation 2 treatments resulted in less than a 1-log decrease. A subsequent experiment extended the incubation period to 4 hours. Viral titers were measured at time zero and after 4 hours of treatment (Fig. 6B). After 4 hours, untreated controls exhibited a 1-log reduction in titer. AgCNP1 treatment markedly reduced OC43 titers from 10^5 to approximately 10^2 $TCID_{50}$ per mL. Both formulation 1 and 3 treatments produced similar reductions, whereas formulation 2 achieved the greatest effect, reducing titers from 10^5 to nearly 10^1 $TCID_{50}$ per mL.

In a separate experiment, OC43 was incubated with nanoparticles at a higher concentration (0.77 mg mL^{-1}) for 3 hours (Fig. 6C), with virus titers assessed at time zero and after 3 hours. The untreated control again showed less than a 1-log reduction. However, treatment with AgCNP1, formulation 2, and formulation 3 reduced OC43 concentrations to undetectable levels. Notably, formulation 1 achieved a 4-log reduction, not inactivating the virus fully but leaving a residual titer of approximately 10^1 $TCID_{50}$ per mL. Collectively, these results suggest that nanoparticle formulations with balanced Ag and CeO_2 content exhibit superior antiviral activity compared to those with more Ag^0- or CeO_2-rich compositions. Superoxide dismutase (SOD)-mimetic activity measurements (Fig. S3) suggest a marked difference in surface chemistry among the tested formulation, with SOD activity appearing to correlate positively with total silver content (72.2 ± 9.62, 33.3 ± 0.01, and 22.2 ± 9.62 for formulations 1.2, 0.5, and 0.2, respectively, at 0.83 μM concentrations). This difference suggests that interaction with reactive oxygen species is not the dominate mechanism in the observed antiviral performance.

Interestingly, the formulations produced in the current study demonstrate comparable efficacy towards virus inactivation, among all formulations and AgCNP1 despite differences in surface composition and particle sizes. This observation, paired with previous observations of AgCNPs outperforming pure cerium oxide nanoparticles of similar character, suggest direct surface interactions between silver and virus particles are not a component in the dominant inactivation mechanism. However, silver contributes an indirect effect, possibly in modifying the ceria particle size or redox state distribution. Further, the substantial difference in average particle size among these tested further suggests that surface curvature is not a significant contributor to the total observed activity.

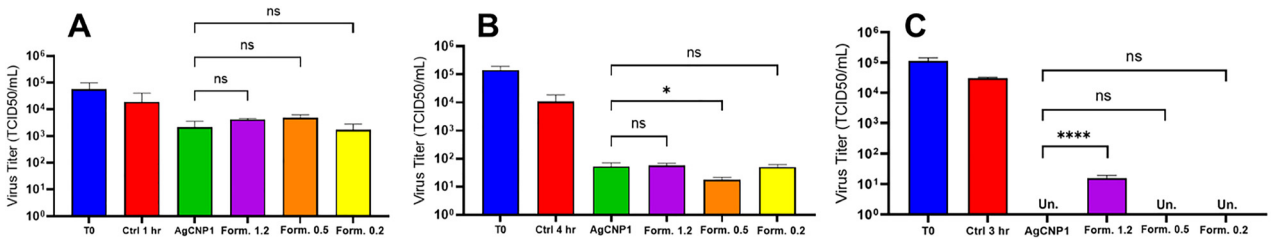

Fig. 6 Effects on virus infectivity. (A) and (B) Samples of OC43 were incubated at room temperature for 1 h (A) or for 4 h (B) with buffer alone (red bars), or with 0.2 mg mL^{-1} AgCNP1 (green), formulation 1.2 (purple), formulation 0.5 (orange), or formulation 0.2 (yellow). Remaining infectivity was determined by TCID50 assay. A sample taken prior to addition of nanoparticles is indicated as time 0 (blue). Values are the mean of three independent samples, with error bars representing the standard deviation. (C) 10^5 TCID50 units of OC43 were incubated at room temperature with buffer alone (blue bars) or the 0.77 mg mL^{-1} AgCNP1. Remaining infectivity was determined after 3 h by $TCID_{50}$ assay. Values are the mean of three independent samples, with error bars representing the standard deviation.

However, the observed results do not preclude the influence of local curvature, potentially arising from the highly granular (rice of the reported rice-ball structure) ceria structure at the particle surface.

Conclusions

In the presented study, several formulations of silver–cerium oxide, core–shell nanostructures were produced and compared for their relative abilities to inactivate a human coronavirus OC43. Formulation syntheses were designed to compare the influences of silver and cerium precursor mixing times and of silver to cerium ratio of precursors. Nanomaterials produced in each formulation possessed unique material with respect to particle size, morphology, and distribution of silver and ceria phases. It was determined that syntheses performed from an initial 1 : 1 mole ratio of silver to cerium precursors produced the smallest and most regular core–shell structures, higher ratios produced larger core–shell structures, while lower ratios produced particles with an increased number of silver phases relative to ceria (similar to a result from our previous studies). Virus inactivation studies of the formulations at 0.2 mg mL^{-1} dosages induced comparable (>2 orders of magnitude reductions) to each other and a high-efficacy formulation from our previous studies, with formulation 2 having the highest performance. The results suggest that virus inactivation by silver–cerium oxide nanostructures is not related to direct virus interaction with silver phases, but that the utility in silver may come from indirect action (such as activating ceria or participating as a co-catalyst).

Author contributions

Craig J. Neal: conceptualization, data curation, formal analysis, investigation, methodology, project administration, writing – original draft. Muhammad Hassan Mehmood Kalyar: investigation, methodology, writing – original draft. Elayaraja Kolanthai: formal analysis, investigation, writing – reviewing & editing. Maria V. Bolen: investigation, data curation, methodology. Griffith D. Parks: methodology, resources, supervision, writing – review & editing. Sudipta Seal: resources, writing – review & editing.

Conflicts of interest

There are no conflicts of interest to declare.

Data availability

The datasets supporting the findings of this study are available within the article and its supplementary information (SI). Supplementary information is available. See DOI: https://doi.org/10.1039/d5ma00962f.

Acknowledgements

CN and EK acknowledge partial funding support from the UCF P3 postdoctoral scholar program. STEM measurements were performed by Dr Nicholas G. Rudawski at the University of Florida's Research Service Center. XPS User facility: NSF MRI: ECCS: 1726636. US National Science Foundation (NSF) REU program EEC: 2050266. Partial funding is acknowledged from NSF IIP: 2208717, and Florida High Tech Corridor.

Notes and references

1 T. X. Sayle, M. Molinari, S. Das, U. M. Bhatta, G. Möbus, S. C. Parker, S. Seal and D. C. Sayle, *Nanoscale*, 2013, **5**, 6063–6073.
2 G. Preda and G. Pacchioni, *Catal. Today*, 2011, **177**, 31–38.
3 F. Benedetti, P. Luches, M. C. Spadaro, G. Gasperi, S. D'Addato, S. Valeri and F. Boscherini, *J. Phys. Chem. C*, 2015, **119**, 6024–6032.
4 P. Luches, F. Pagliuca, S. Valeri, F. Illas, G. Preda and G. Pacchioni, *J. Phys. Chem. C*, 2012, **116**, 1122–1132.
5 J. S. Pelli Cresi, E. Principi, E. Spurio, D. Catone, P. O'Keeffe, S. Turchini, S. Benedetti, A. Vikatakavi, S. D'Addato and R. Mincigrucci, *Nano Lett.*, 2021, **21**, 1729–1734.
6 J. S. Pelli Cresi, E. Silvagni, G. Bertoni, M. C. Spadaro, S. Benedetti, S. Valeri, S. D'Addato and P. Luches, *J. Chem. Phys.*, 2020, **152**, 114704.
7 E. Aneggi, J. Llorca, C. de Leitenburg, G. Dolcetti and A. Trovarelli, *Appl. Catal., B*, 2009, **91**, 489–498.
8 B. Matovic, S. Butulija, Z. Dohcevic-Mitrovic, T. M. Arsic, J. Lukovic, S. Boskovic and J. Maletaskic, *J. Eur. Ceram. Soc.*, 2020, **40**, 1983–1988.
9 T. Mitsudome, M. Matoba, T. Mizugaki, K. Jitsukawa and K. Kaneda, *Chem. – Eur. J.*, 2013, **19**, 5255–5258.
10 T. Mitsudome, Y. Mikami, M. Matoba, T. Mizugaki, K. Jitsukawa and K. Kaneda, *Angew. Chem., Int. Ed.*, 2012, **51**, 136–139.
11 T. Kayama, K. Yamazaki and H. Shinjoh, *J. Am. Chem. Soc.*, 2010, **132**, 13154–13155.
12 C. J. Neal, C. R. Fox, T. S. Sakthivel, U. Kumar, Y. Fu, C. Drake, G. D. Parks and S. Seal, *ACS Nano*, 2021, **15**, 14544–14556.
13 C. R. Fox, K. Kedarinath, C. J. Neal, J. Sheiber, E. Kolanthai, U. Kumar, C. Drake, S. Seal and G. D. Parks, *Molecules*, 2023, **28**, 5190.
14 A. González, C. Noguez, J. Beránek and A. Barnard, *J. Phys. Chem. C*, 2014, **118**, 9128–9136.
15 R. M. Pallares, S. L. Karstens, T. Arino, A. M. Minor and R. J. Abergel, *ACS Appl. Nano Mater.*, 2023, **6**, 8141–8145.
16 F. Muhammad, F. Huang, Y. Cheng, X. Chen, Q. Wang, C. Zhu, Y. Zhang, X. Yang, P. Wang and H. Wei, *ACS Nano*, 2022, **16**, 20567–20576.